Key Points:
- Slow Slip Event recurrence rate was unaffected by large earthquake on same megathrust segment
- Deep and shallow zones of SSE behaved differently following the earthquake
- Change in slip magnitudes for SSE show variability in strain release through SSE during the earthquake cycle

Slow slip events in the early part of the earthquake cycle

Nicholas K. Voss[1] (ID), **Rocco Malservisi[1]** (ID), **Timothy H. Dixon[1]** (ID), and **Marino Protti[2]** (ID)

[1]School of Geosciences, University of South Florida, Tampa, Florida, USA, [2]Observatorio Vulcanológico y Sismológico de Costa Rica, Universidad Nacional, Heredia, Costa Rica

Abstract In February 2014 a $M_w = 7.0$ slow slip event (SSE) took place beneath the Nicoya Peninsula, Costa Rica. This event occurred 17 months after the 5 September 2012, $M_w = 7.6$, earthquake and along the same subduction zone segment, during a period when significant postseismic deformation was ongoing. A second SSE occurred in the middle of 2015, 21 months after the 2014 SSE and 38 months after the earthquake. The recurrence interval for Nicoya SSEs was unchanged by the earthquake. However, the spatial distribution of slip for the 2014 event differed significantly from previous events, having only deep (~40 km) slip, compared to previous events, which had both deep and shallow slip. The 2015 SSE marked a return to the combination of deep plus shallow slip of preearthquake SSEs. However, slip magnitude in 2015 was nearly twice as large ($M_w = 7.2$) as preearthquake SSEs. We employ Coulomb Failure Stress change modeling in order to explain these changes. Stress changes associated with the earthquake and afterslip were highest near the shallow portion of the megathrust, where preearthquake SSEs had significant slip. Lower stress change occurred on the deeper parts of the plate interface, perhaps explaining why the deep (~40 km) region for SSEs remained unchanged. The large amount of shallow slip in the 2015 SSE may reflect lack of shallow slip in the prior SSE. These observations highlight the variability of aseismic strain release rates throughout the earthquake cycle.

Plain Language Summary We analyzed small signals in continuous GPS time series. By averaging many GPS measurements over a day, we are able to get very precise measurements of the motion of the ground. We found two events in the Nicoya Peninsula of Costa Rica where the GPS changed direction and began moving toward the oceanic trench in the opposite direction of subduction plate motion. These events are called slow slip events and have been found in other regions such as Cascadia, Alaska, Japan, and New Zealand. In Nicoya, a large earthquake of magnitude 7.6 on the Richter scale occurred in 2012. The two slow slip events occurred in 2014 and 2015. We explored the relationship between the earthquake and the slow slip events and looked to see if the earthquake changed the behavior of the slow slip events. We found that the slow slip events have a regular timing before and after the earthquake, but the behavior of the slow slip events since the earthquake is different with slip taking place along different portions of the plate interface then was previously seen.

1. Introduction

Slow slip events (SSEs) have now been observed in many subduction zones [e.g., *Dragert et al.*, 2001; *Lowry et al.*, 2001; *Obara*, 2002; *Douglas et al.*, 2005; *Schwartz and Rokosky*, 2007]. However, they remain enigmatic for several reasons, including spatially limited and temporally aliased observations. Many SSEs occur offshore, beyond the reach of on-land geodetic observations. We also lack a long-term record of these events, for example, over a full seismic cycle. Hence, their role in the overall strain accumulation-release budget for subduction zones, and whether they can be used for hazard forecasting (e.g., do slow slip events trigger earthquakes?) is difficult to evaluate [*Obara and Kato*, 2016].

Available data are largely limited to the middle or late parts of the earthquake cycle and to the downdip portion of the seismogenic zone, although seafloor geodetic data offshore Tohoku may also provide an opportunity to study earthquake cycle effects on SSE [*Ito et al.*, 2013]. The area of Nicoya in Costa Rica is an exception to this. Prior to the 2012 earthquake, SSE events in Nicoya were detected in two regions: a deep region (40 km depth) of the plate interface beneath the Gulf of Nicoya, and a shallow region (10–20 km depth) just off the coast [*Dixon et al.*, 2014]. The geodetic network was able to detect slip due to SSE after the M_w 7.6 megathrust event of 4 September 2012. Here we describe two SSEs in the early part of the earthquake cycle. The first event occurred beneath the Nicoya peninsula of Costa Rica in 2014, 1.5 years after the 2012 earthquake. The second event occurred 2 years later in October 2015. Slip distribution estimates for the 2014 event indicate that slip occurred beneath the Gulf of Nicoya,
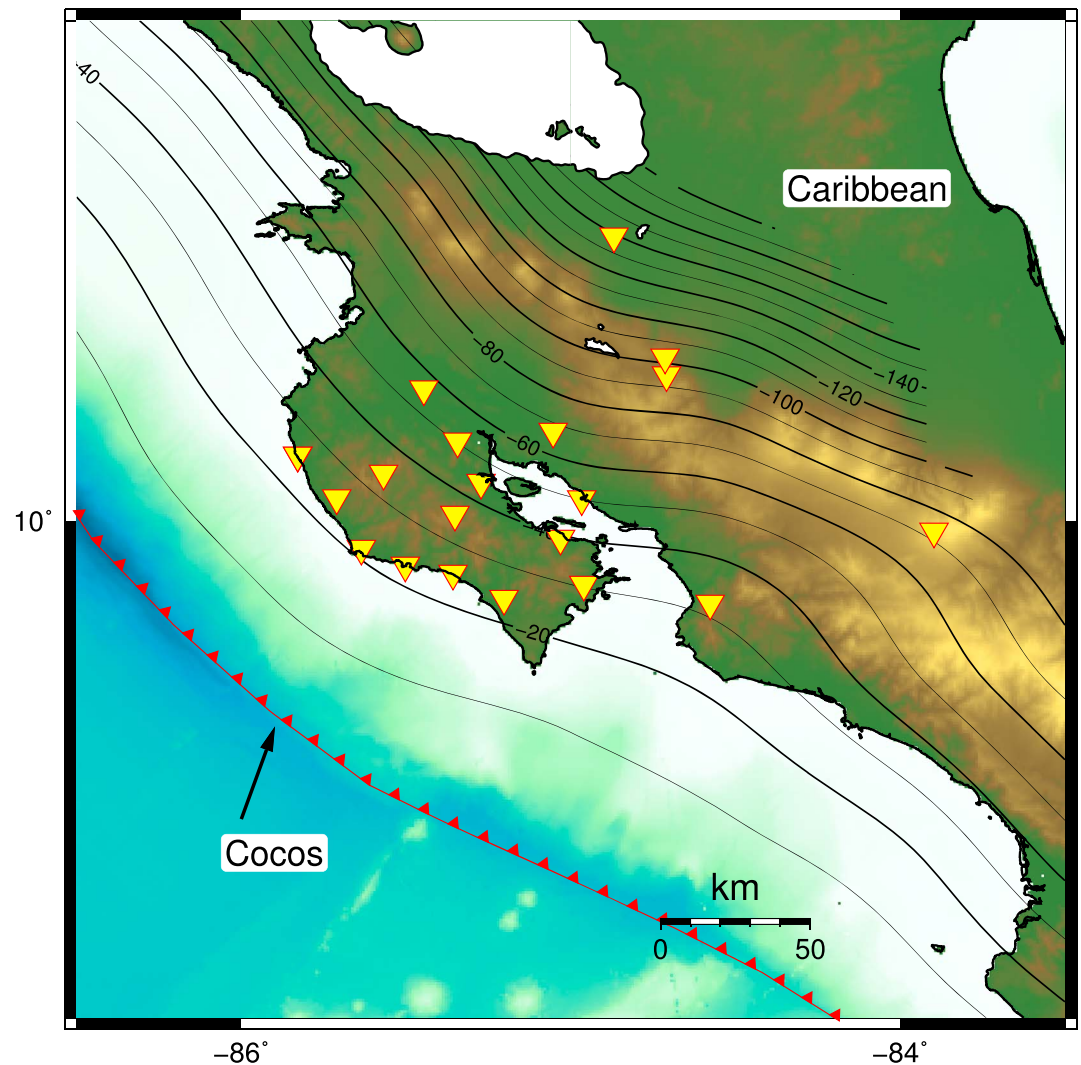
Figure 1. Tectonic map of Costa Rica. Yellow triangles indicate location of GPS stations. Contours mark 10 km intervals of slab depth according to Slab1.0 [*Hayes et al.*, 2012].

centered at a depth of 40 km. This deep slip patch is consistent with observations of deep slow slip in Nicoya prior to the earthquake [*Dixon et al.*, 2014]. Shallow (10–20 km depth) slip magnitudes during the 2014 event were considerably less than events observed during the late interseismic portion of the earthquake cycle. During the 2015 event, high slip magnitudes returned to the shallow portion of the plate interface, with spatial distribution matching that of large preearthquake SSEs. However, total moment release during this second SSE was considerably larger, almost double that of previously observed SSEs. We hypothesize that the combination of coseismic slip and afterslip produced stress changes at the nucleation site of shallow slow slip events, making conditions for their generation unfavorable. We employ Coulomb stress modeling to explain the lack of shallow slow slip in 2014 and the persistence of deep slow slip throughout the earthquake cycle and discuss the interplay between earthquakes, afterslip, and aseismic slip.

2. Geologic Setting and Geodetic Network

High precision GPS instruments in the Nicoya Peninsula of Costa Rica have facilitated detailed geodetic observations of key parts of the earthquake cycle: late interseismic [*Dixon et al.*, 2014; *Jiang et al.*, 2012; *Feng et al.*, 2012], coseismic [*Protti et al.*, 2014], and early postseismic stages [*Malservisi et al.*, 2015]. The peninsula lies along the Middle America subduction zone, where the Cocos plate is subducted beneath the Caribbean plate at a rate of 8 cm/yr (Figure 1) [*DeMets*, 2001]. The top of the subducting slab is ~20 km below the coast of the

peninsula, and the peninsula overlies the main seismogenic zone, allowing good geodetic resolution of this critical area of the megathrust interface with onshore instruments. A network of GPS stations began to be installed in the early 2000s, and the first SSE was recognized in 2003 [*Protti et al.*, 2004; *Davis and Villinger*, 2006]. With densification of the network by 2007, now consisting of 18 stations, detailed images of slip distribution during SSEs became possible, [*Outerbridge et al.*, 2010]. In 2012, a magnitude 7.6 earthquake took place within a previously identified locked zone [*Feng et al.*, 2012; *Protti et al.*, 2014; *Xue et al.*, 2015]. Our new observations provide an opportunity to explore how SSEs contribute to strain accumulation and release in the subduction zone during the early stage of the earthquake cycle, and their relation to megathrust earthquakes.

3. Data Processing

GPS data are processed using GIPSY-OASIS 6.4 software with orbits and satellite clock estimates from the Jet Propulsion Laboratory (JPL). Daily static positions were calculated using the Precise Point Positioning method [*Zumberge et al.*, 1997]. Phase ambiguity resolution was performed using the single receiver algorithm [*Bertiger et al.*, 2010]. Ocean loading corrections were applied using FES2004 [*Lyard et al.*, 2006]. VMF1 mapping functions were used to estimate and correct for the tropospheric delay [*Boehm et al.*, 2006]. Second-order ionosphere corrections were done using the IONEX model [*Bassiri and Hajj*, 1993; *Kedar et al.*, 2003]. Daily solutions were computed in a loosely constrained reference frame, then aligned with IGb08 [*Rebischung et al.*, 2012] using daily seven parameter transformation files provided by JPL. The final products are time series of daily positions for each component (north-south, east-west, and up-down).

4. Seasonal Signal Removal

Identifying SSEs and quantifying their slip history require careful separation of noise and various signals in the time series. This can be challenging because SSE signals may approach the level of GPS noise. Iterative techniques are often employed but can involve trade-offs among estimated parameters. When the observation network is sufficiently large and observed transients are only present on a subset of the network, spatial filtering can be used to reduce common mode noise [*Wdowinski et al.*, 1997]. However, for smaller networks, if the deformation transient is present at all stations, then stacking and subsequent common mode noise removal may alter the observed signal. Seasonal signals related to atmospheric effects can also be a challenge. Commonly, fixed amplitude sine and cosine functions are fit via least squares to the time series and then removed [e.g., *Jiang et al.*, 2012]. This can lead to artifacts if seasonal amplitudes vary.

A new approach to noise and parameter estimation, termed Multi-channel Singular Spectrum Analysis (MSSA) [*Walwer et al.*, 2016] enables simultaneous identification of common mode signals and time-varying seasonal signals. MSSA takes advantage of the spatial correlations within the network by incorporating multiple data channels, similar to Principle Components Analysis (PCA), which is equivalent to MSSA when the time lag is 0 [*Dong et al.*, 2006]. MSSA is also efficient at recognizing temporal correlations (such as seasonal signals) through calculation of the covariance of time lagged copies of the original time series using a modification of singular spectrum analysis (SSA) [*Chen et al.*, 2013]. This approach allows for simultaneous extraction of information on spatial and temporal correlations within the network [*Walwer et al.*, 2016]. This is an expansion of the PCA technique which is efficient at recognizing spatial correlations [*Dong et al.*, 2006] and SSA which is used for the recognition of temporal correlation with a single channel. MSSA deals with both spatial and temporal correlations and has the advantage of not requiring a priori assumptions about the nature of the time series [*Walwer et al.*, 2016]. It can thus adjust for variable amplitude seasonal signals.

MSSA begins with the creation of data matrix blocks $X_{1,...,L}$ for each component of each GPS station where $L = c \times n$, where c the number of GPS components analyzed and n is the number of stations. The first column of each block X_l contains a copy of the original time series of length $N - M + 1$ with N equal to the number of epochs and M is the maximum time lag. Each subsequent column is formed by applying a time lag of one epoch to the original time series, out to a time lag of M [*Ghil et al.*, 2002]:

$$X_l = \begin{bmatrix} x_0^l & x_1^l & \cdots & x_M^l \\ x_1^l & x_2^l & \cdots & x_{M+1}^l \\ \vdots & \vdots & \ddots & \vdots \\ x_{N-M+1}^l & x_{N-M+2}^l & \cdots & x_N^l \end{bmatrix} \qquad (1)$$
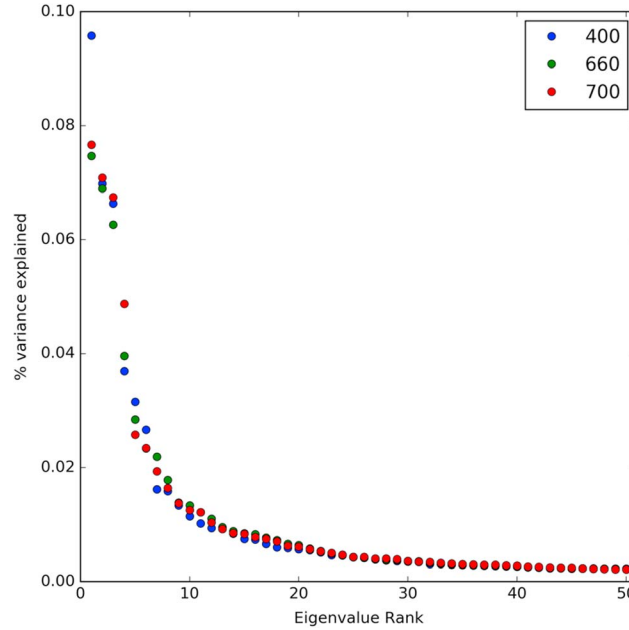
Figure 2. Normalized eigenvalue spectrum for different window lengths (time lag, M). Choice of window length does not significantly affect the analysis.

where $[x_1^l, x_2^l, \cdots, x_N^l]$ is the time series for one component of a single station and $l = 1, 2, …, c*n$. Ideally, M should be longer than the longest period signal to be identified, but an empirical estimation by trial and error is effective.

The full trajectory matrix D is formed through the combination of all the matrices X_l (one for each GPS station and component) [*Broomhead and King*, 1986; *Allen and Robertson*, 1996]:

$$D = (X_1 \, X_2, …, X_L) \qquad (2)$$

Matrix D has L columns and $N - M + 1$ row. The matrix D can then be used to find the symmetric $M \times M$ lagged covariance matrix C:

$$C = \frac{1}{N - M + 1} D^T D \qquad (3)$$

Eigenvalue decomposition of the matrix C produces eigenvalues λ_k and eigenvectors E^k indicating the magnitude of variance along the components of a given base of the vector space of the signal. The eigenvalues λ_k provide an indication of the variance associated with their corresponding principal. Ordering from the largest to the smallest the eigenvalues and corresponding eigenvectors is then equivalent to ordering the components of the observed signal in order of decreasing variance. (Figure 2). Principal components, A^k, are then calculated through the projection of the data matrix X onto the eigenvectors E:

$$A_t^k = \sum_{j=1}^{M} \sum_{l=1}^{L} x_{t+j-1}^l E_j^k \qquad (4)$$

where t is the time index ($t = 1, 2, …, N - M$), k is the rank of the eigenvalue ($k = 1, 2, …, M$), j is the time lag ($j = 1, 2, …, M$), and l is a GPS component time series ($l = 1, 2, …, c*n$). Each times series, x^l, can then be partially reconstructed using the kth principal component [*Vautard et al.*, 1992]:

$$\widetilde{x}_t^{k\,l} = \begin{cases} \dfrac{1}{M} \sum_{j=1}^{M} A_{t-j+1}^k E_l^k & M \le t \le N - M + 1 \\[3mm] \dfrac{1}{t} \sum_{j=1}^{i} A_{t-j+1}^k E_l^k & 1 \le t \le M - 1 \\[3mm] \dfrac{1}{N - t + 1} \sum_{j=1-N+M}^{M} A_{t-j+1}^k E_l^k & N - M + 2 \le t \le N \end{cases} \qquad (5)$$

The summation of all reconstructed components, $\widetilde{x}^{k\,l}$, reconstructs the original data x^l. [*Walwer et al.*, 2016].

We performed MSSA on all available time series from January 2007 through June 2016. The predominant signals in each time series correspond to a linear trend reflecting interseismic strain accumulation, offsets due to the 2012 earthquake, and postseismic signals. In order to highlight the variance associated with SSEs, we removed these signals prior to MSSA analysis by fitting each time series independently using the following equation via least squares:

$$u_i(t) = a + bt + \sum_{j=1}^{m} g_j H(t - t_j) + \sum_{i=1}^{3} k_i \left(1 - e^{\frac{t - T_o}{\tau_i}}\right) \qquad (6)$$

where a is a bias mainly related to the assumed reference epoch, b is the interseismic rate (the tectonic velocity during the interseismic period), $H(t - t_j)$ is the Heaviside function to take into account the coseismic
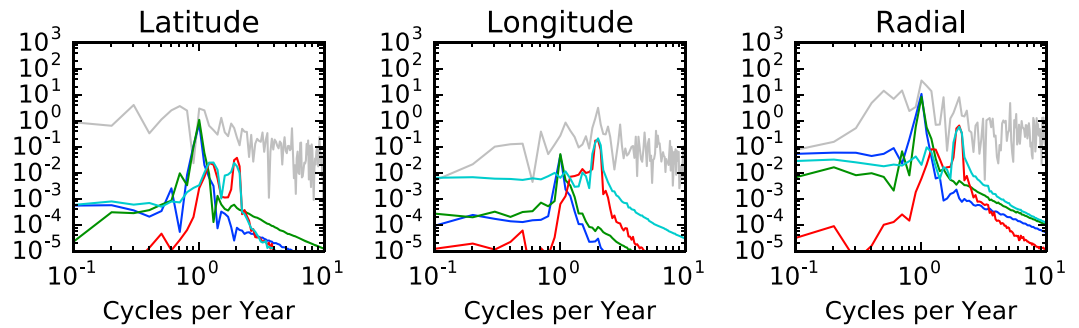
Figure 3. Power spectral density plots for station BIJA for the east, west, and vertical components. The grey colors are the raw time series. Dark blue is the reconstructed time series using the second principal component. Green is the reconstructed time series using third principal component. These components show a clear peak at 1 c/yr. Light blue and red represent the reconstructed thirteenth and fourteenth principal.

displacement or instrument substitution time t_j, and g_j is the amplitude of offset due to equipment changes and earthquakes. The last terms correspond to transients associated with postseismic deformation. Following *Malservisi et al.* [2015], we assume that these decay exponentially with three characteristic times τ_i, and amplitudes k_i. Decay times (7, 70, and 420 days) are taken from *Malservisi et al.* [2015] and are not estimated during the fitting process. Displacement amplitudes related to each time decay time at each station and component can be found in Table S1 in the supporting information.

Significant gaps in our time series exist, reflecting growth of the network and equipment failures (Figure S1). These gaps are filled using Gaussian random noise with zero mean and unit standard deviation [*Walwer et al.*, 2016; *Unal and Ghil*, 1995]. While the filled time series do not have the same spectral properties as the original GPS time series, choice of a Gaussian random noise filler causes the variance associated with the gap associated in the time series to be associated with lower ranked eigenvalues such that they do not bias the seasonal signal estimate. We apply a window of length (time lag) M of 660 days, chosen to capture the periodic signals associated with SSEs which have typical repeat times of 620 days. Tests using different window lengths between 400 and 700 days did not significantly affect results (Figure 2).

The eigenvalue spectrum decays slowly, as is common when using a long sliding time window, reflecting a spreading of features across multiple eigenvalues [*Vautard and Ghil*, 1989]. For eigenvalues with rank larger than 30, the spectrum levels off, signaling that the majority of the signal in the network time series can be represented using only the first 30 principal components (PCs). However, due to the slow decay, we include all PCs which do not contain seasonal periods. Through analysis of the power spectral density of the PCs (Figure 3), we identify four components that contain frequency at the annual (PCs 2 and 3) and semiannual (PCs 13 and 14) periods. These seasonal signals are large in tropical regions such as Costa Rica, presumably reflecting atmospheric effects [*Mao et al.*, 1999].

In order to remove the seasonal signal, we reconstruct the time series for each component, excluding PCs 2, 3, 13, and 14, equivalent to extracting the signals associated with the PCs 2, 3, 13, and 14 from the original data set. The residual time series contain transient signals not associated with seasonal periods, as well as noise. In the following analysis we use the reconstructed time series for a study of SSE behavior (Figure 4).

The MSSA technique does not provide any information about the physical processes governing specific principal components. As such, a portion of the signal contained within the excluded principal components could be related to tectonic signals but represent a much smaller portion of the overall time series variance. MSSA performs slightly better than traditional fixed sine and cosine analysis of seasonal signals [*Chen et al.*, 2013]; however, the analysis of the SSE behavior that follows is consistent regardless of filtering approach.

5. SSE Identification

SSE onset was initially identified through visual inspection of the raw GPS displacement time series. The displacement at each time step was then modeled as the residual inter SSE trend, and hyperbolic tangent function representing SSEs [*Larson et al.*, 2007]. The equation takes the form.
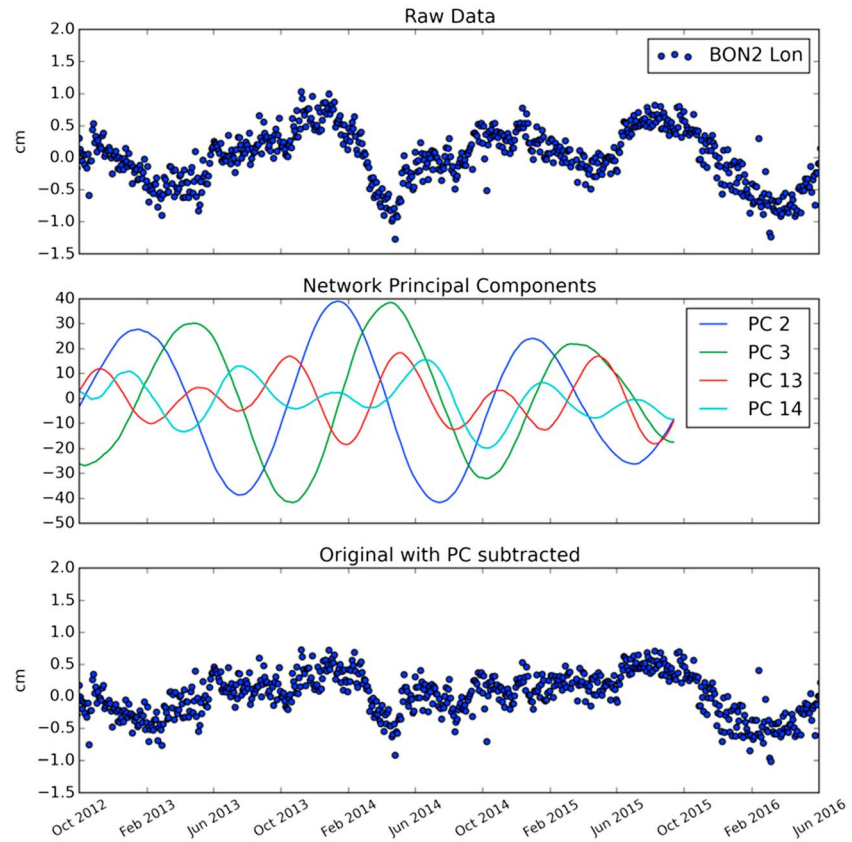
Figure 4. Example time series. (top) The longitudinal component of station BON2, with postseismic signals removed. (middle) The principal components associated with seasonal signals. (bottom) The residual time series after removing the seasonal components.

$$u(t) = a + bt + \sum_{k=1}^{n} \frac{U_k}{2} \left(\tanh \frac{t - T_k}{\tau_k} - 1 \right) \tag{7}$$

where a is the offset at the assumed reference epoch, b is the inter-SSE rate, U_k describes the amplitude of the kth SSE, T_k is the given SSE midpoint time, and τ_k is its duration. This model is fit to the time series using the Levenburg-Marquart algorithm as implemented in Python package lmfit (http://lmfit.github.io/lmfit-py/). Parameter bounds are used for estimation of T_k and τ_k based on visual inspection, with values estimated as part of the iterative inversion process. Figure 5 shows an example of the full displacement model and the various components modeled and removed. Table S2 shows the resulting displacement estimates and one standard error.

6. Slow Slip Recurrence

The 2014 SSE started in early February and lasted ~1.5 months, 20 months after the preceding SSE, which had occurred immediately prior to the 2012 earthquake [*Dixon et al.*, 2014]. The 2015 SSE started in October and lasted ~7 months, similar to an SSE that occurred in 2009. Given the 12 year record in Costa Rica, we can calculate the average recurrence interval for SSEs. Small events, below our assumed detection threshold of M 6.5, are excluded as their identification is dependent on network density (Figure S1). The recurrence rate of SSEs has decreased with the increasing number of stations which we attribute to better detection capabilities. If we take into account the smaller events identified during the late interseismic period, the variability in SSE recurrence is much larger. These events have varying slip distributions and have also proven difficult to reliably detect [*Jiang et al.*, 2012, *Dixon et al.*, 2014]. Following the earthquake, ongoing postseismic deformation may mask these smaller SSEs. Eight large events ($M > 6.5$) have been recorded by the network
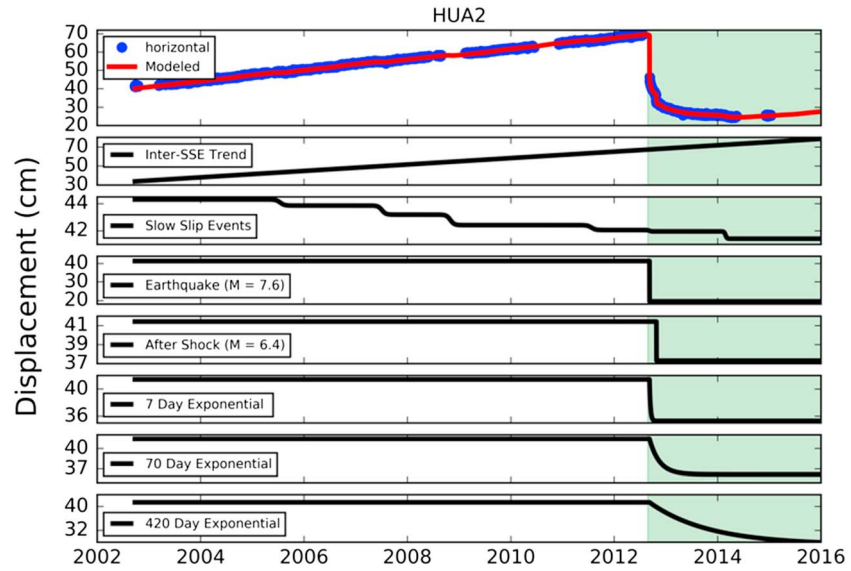
Figure 5. Example time series showing relative contributions of tectonic signals since GPS station HUA2 was installed. Blue is measured GPS displacement; red is modeled displacement. Black lines represent displacements due to known or modeled tectonic signals. Sum of all the black lines shown gives the modeled displacement shown in the top panel (red).

(Figure 6). Two of them are large events prior to 2007, identified by both GPS and offshore boreholes as pressure transients [*Davis et al.*, 2011]. In order to reduce biases due to the variation of detection threshold of the different events, we choose to analyze the recurrence interval using only these larger events. These events have similarities in both slip distribution and their larger signal-to-noise ratio. Nevertheless, it is important to note that the small number of observed events affects the following statistical analysis.

One way to investigate the earthquake effects on the recurrence interval of SSEs is to consider whether the system is in steady state. If the system is in steady state, then previous SSE timing can be used to predict the timing of future SSEs. We use the Kolmogorov-Smirnov (K-S) test statistic (D_n) [*Chakravarty et al.*, 1967] to determine if recurrence rates in Nicoya are in steady state. In this case we test the difference between the observed distribution and a uniform distribution, i.e., constant recurrence rate:

$$D_n = \max_{t \in [S,T]} \left[\left| F_n(t) - \frac{t-S}{T-S} \right| \right] \tag{8}$$

where t is time, S is start time, T is end time, and n is total number of events haven taken place at time t. The observed distribution F_n is given by

$$F_n = \frac{\#(t_i \leq T)}{n}, i = 1, \ldots, n, S < t < T \tag{9}$$

The null hypothesis can be rejected if $D_n > \frac{1.36}{\sqrt{N(S,T)}}$ at the 95% confidence level [*Zwillinger and Kokoska*, 1999].

In this case N(S,T) is 11 events if we use all known SSEs starting with the first event in August 2003 through the final event in October 2015. D_n is 0.07, and the system is clearly in steady state (Figure S1). Thus, we can assume that previous events provide information on the recurrence of future events, an admittedly easy criterion given the relatively small number of events.

The average recurrence interval for $M > 6.5$ SSE observed between 2007 and 2015 is 20.5 ± 5.5 months. The standard deviation is largely controlled by the 2011 event. This event was preceded by an unusually long duration (6 month) event in 2009 [*Jiang et al.*, 2012], which may explain its delayed onset. If that event is excluded, the standard deviation is reduced to 1.2 months with no change in the mean. This value (20.5 months) is very similar to the previously identified recurrence interval (21 months) before the earthquake [*Jiang et al.*, 2012]. Thus, the 2014 and 2015 slow slip events appear to have occurred "on schedule" with no delay in timing induced by the 2012 earthquake.
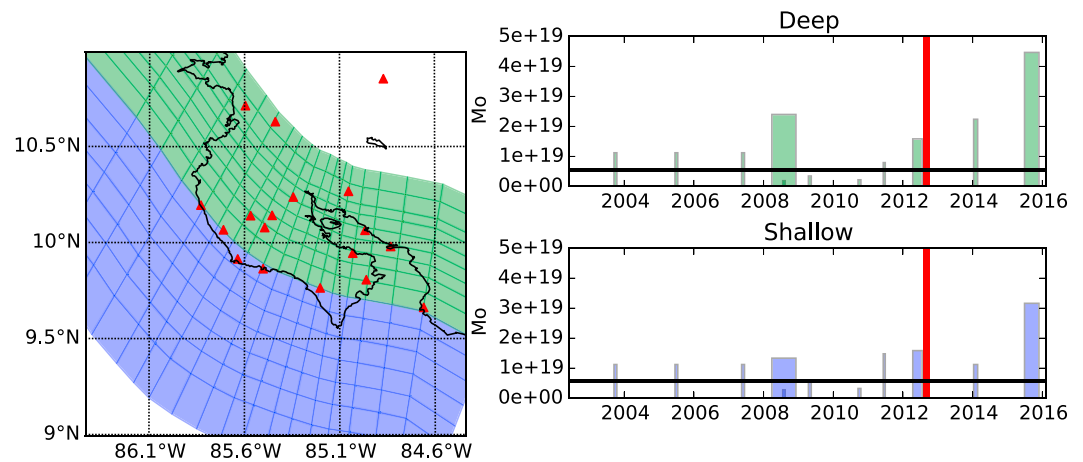
Figure 6. Timeline and Magnitude of Nicoya SSEs. (left) GPS network operating in 2014 is shown by red triangles. (right) Red vertical bar marks the 2012 earthquake. Black horizontal line marks the assumed M6.5 SSE detection threshold. The separation between shallow and deep is defined as the 24 km depth contour of the Slab1.0 fault model [*Hayes et al.*, 2012] and is indicated by green for the shallow shaded region and bars and blue for the deep shaded region and bars.

The periodic behavior of SSEs has been simulated with 2-D and 3-D models of the earthquake cycle using a rate-and-state friction framework [*Matsuzawa et al.*, 2010; *Colella et al.*, 2012]. These models predict a shortening of the SSE recurrence interval as the earthquake cycle progresses [*Matsuzawa et al.*, 2010] and resulting stress concentration at the base of the seismogenic zone [*Colella et al.*, 2012]. Evidence of recurrence interval shortening has been seen along the Boso peninsula, although the mechanism is still unclear [*Ozawa*, 2014; *Hirose et al.*, 2012]. In Nicoya this is not observed for the large SSE: the observed recurrence interval for large SSE is similar before and after the earthquake. It is worth to note that an increase of events just before the main shock of 2012 can be observed including the small events, but we are not able to distinguish if the variation in periodicity is merely a result of a change in detection threshold.

7. Slip Inversion

In order to investigate the spatial extent of the early earthquake cycle SSEs and compare to previous events, we use the observed GPS displacements to invert for slip on the subduction interface. We use the plate geometry described by Slab1.0 [*Hayes et al.*, 2012] discretized into 18 along strike and 15 along dip patches of approximately 30 km^2. Slip on the patches is then related to surface displacements using an analytical solution for rectangular dislocations in a half-space [*Okada*, 1992]. Slip direction is constrained to positive rakes; e.g., only thrust and strike slip motion is allowed. Rake is allowed to vary between patches. We use the Levenburg-Marquart algorithm implemented in the PEST software [*Doherty*, 2012] to perform the inversion. PEST uses the Gauss-Newton algorithm to form a trust region between the Newton search direction and the gradient descent direction in the parameter space [*Aster*, 2013]. The trust region represents the region of the space of parameters where the objective function is well approximated by the model function. In order to attain physically reasonable results, Tikhonov regularization is implemented through minimization of parameter differences. The objective function minimized represents the sum of contributions from the regularization equations and the measured displacements. The measurement displacements are weighted inversely proportional to their estimated one standard error as estimated from the Levenburg-Marquart algorithm, and both horizontal and vertical observations are used. Errors for the horizontal components and vertical components average 5 mm and 20 mm, respectively. A target measurement objective function is set such that the cumulative residual approaches the assumed measurement error. This solution is equivalent to the minimum error variance solution and enforces the regularization conditions to the maximum extent possible within the assumed observation noise [*Doherty and Hunt*, 2010].

7.1. The 2014 SSE Slip Distribution

The 2014 event is characterized by a deep slip patch coinciding with the 45 km depth contour on the upper slab interface, with a peak slip of 135 mm ($M_w = 7.0$) underneath the Nicoya Gulf (Figure 7). The slip associated
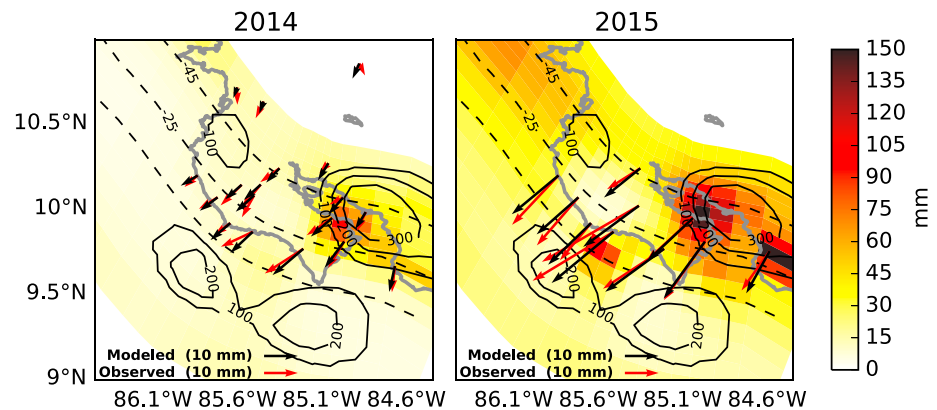
Figure 7. Slip Distributions for the SSEs. The (left) 2015 SSE and (right) 2014 SSE slip distributions. Color scale is slip magnitude in millimeters. Black contours mark cumulative slip identified in previous SSE in the region contoured in units of millimeter [*Dixon et al.*, 2014]. Dotted lines mark the 10 km, 25 km, and 45 km contours of slab depth.

with the 2014 event is similar in both location and magnitude to the slip observed for the deep patch of the events observed in 2007, 2009, and 2012 SSEs [*Outerbridge et al.*, 2010, *Dixon et al.*, 2014]. This deep patch of SSEs is located downdip from an asperity that ruptures every ~50 years and last ruptured during the 1990 *M* 7 earthquake [*Protti et al.*, 1995]. Noticeably absent is the offshore shallow slip patch (~10–15 km depth) that is persistent in earlier events [*Dixon et al.*, 2014]. Relaxation of regularization conditions sufficiently fit the data with a single condensed region of slip in the center of the deep patch, with zero slip in the offshore region. This solution greatly over fits the data resolution but provides insight into the dominant slipping area during 2014. The predominance of uplift across the network during the 2014 event, as well as the relative onset time of the events in the different GPS time series (the observed signal onset migrates trenchward) are consistent with lack of shallow slip in 2014 (Figure S2). This contrasts with previous large SSEs in Nicoya which all contained some degree of shallow slip [*Outerbridge et al.*, 2010; *Dixon et al.*, 2014]. This behavior reinforces the idea of different mechanisms for deep (>25 km) versus shallow (<20 km) SSEs [*Outerbridge et al.*, 2010], which span quite different temperature and pressure conditions. In comparison, the 2012 earthquake took place directly beneath the peninsula [*Yue et al.*, 2013; *Protti et al.*, 2014], while the afterslip extended primarily updip of the main rupture [*Malservisi et al.*, 2015]. The downdip limit of the seismogenic zone of large regular megathrust earthquakes under Nicoya lies at 30–35 km depth, suggesting that deep SSEs are taking place in the transition zone from locked to continuous creep.

7.2. The 2015 SSE Slip Distribution

The 2015 event is similar to the large events prior to the 2012 earthquake; however, it is significantly larger, *M* = 7.2 (Figure 7). Observed displacements are approximately double what was observed in 2014. However, the size and duration of the 2015 event are consistent with global averages of moment-duration scaling [*Ide et al.*, 2007]. Coastal stations see significant deformation (Figure S2) indicating that shallow slip occurred between 10 and 20 km depth likely on the plate interface. The persistent deep patch is still located beneath the Nicoya Gulf, as in 2014 and preearthquake SSEs. The shallow zone of slow slip appears to be just off the coast, not coincident with shallow slow slip during preearthquake SSEs [*Outerbridge et al.*, 2010, *Dixon et al.*, 2014]. Tests of the inversion implementation with displacements from *Dixon et al.* [2014] are consistent with their results. The shallow patch in 2015 appears to be in between the two zones of shallow slow slip observed during the preearthquake period. This zone is coincident with the location of a *M* 6.6 aftershock that occurred on 24 October 2012 [*Malservisi et al.*, 2015]. Model resolution decays significantly with distance offshore (Figure S3) [*Dixon et al.*, 2014; *Kyriakopoulos and Newman*, 2016]. However, the region adjacent to the coast has good resolution. The northwest corner of the megathrust appears to experience moderate amounts of slip (~60–70 mm). However, there are no observations near this region of the fault so interpretation is difficult. Relaxation of regularization conditions does not remove the need for slip in this region, and it appears to be similar to a region where slip occurred in 2007 and 2009 when observations were available immediately above the fault in this zone [*Dixon et al.*, 2014].
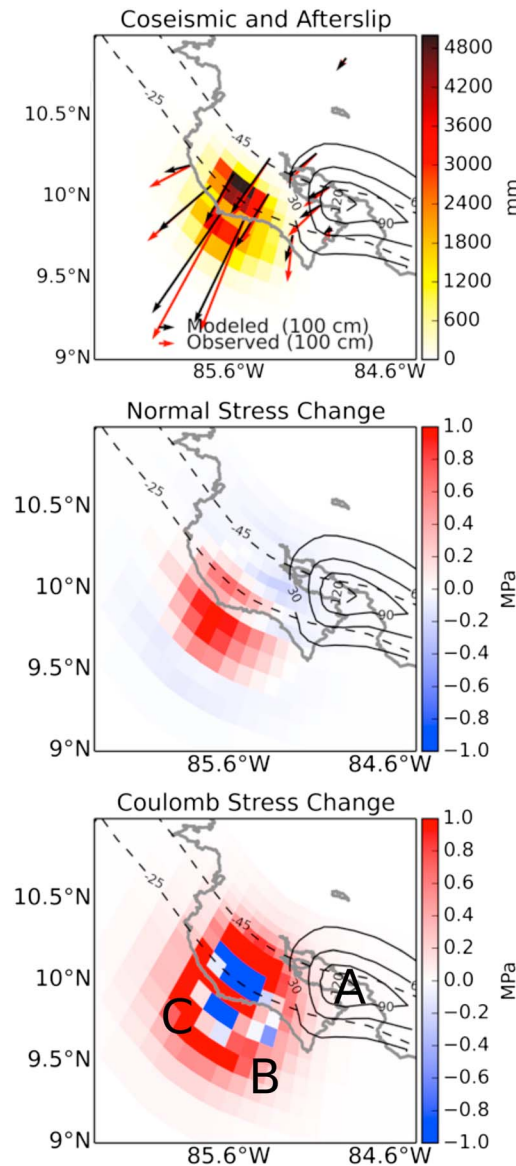
Figure 8. (top) Slip distribution from the combined 2012 earthquake, aftershock, and afterslip. (middle) Fault normal stress change associated with the slip distribution. (bottom) Coulomb stress change assuming pure thrust motion. Black contours outline the slip from the 2014 SSE. A labels the location of the deep SSE patch, B labels the location of the southeastern shallow patch, and C labels the location of the northwestern shallow patch.

8. Influence of Coulomb Failure Stress Changes on SSE Slip Distribution and Occurrence Time

In order to describe the differing modes of strain accumulation and release on the subduction interface, it is useful to consider zones of differing stress states and frictional properties [*Scholz*, 1998]. Portions of the subduction zone where SSEs occur are often described as conditionally stable, since transient creep (SSE) occurs and earthquakes can propagate although not nucleate [*Schwartz and Rokosky*, 2007]. This zone is often considered critically stressed due to its response to small changes in stress associated with tides and other loading phenomena [*Lambert et al.*, 2009; *Shen et al.*, 2005]. If SSEs respond to stresses as small as 0.015 MPa (0.15 bar) [*Rubinstein et al.*, 2008], then it stands to reason that they should respond to stress changes from the 2012 earthquake. To test this, we take the integrated slip from the combination of the earthquake, afterslip associated with the 70 day relaxation time [*Malservisi et al.*, 2015] and the 24 October aftershock, and then calculate the corresponding change in Coulomb Failure Stress (ΔCFS) on the plate interface (Figure 8) [*Reasenberg and Simpson*, 1992; *Stein et al.*, 1992; *Toda et al.*, 2011]. Positive values imply increased chance of failure, while negative values imply a reduced chance of failure. We use the slip distribution from the coseismic, aftershock, and afterslip inversion with the same model

geometry. In these calculations, we assume a rake of 90° similar to the rake of the modeled SSE and $\mu' = 0.4$. Changes in rake direction consistent with thrust faulting do not significantly affect the calculated ΔCFS. We find that cumulative slip from the earthquake, afterslip, and aftershock induces ΔCFS of +0.01 MPa on the deep patch (A in Figure 8), +0.05 MPa on the southeastern portion of the shallow patch (B in Figure 8), and +0.8 MPa on the northern shallow patch (C in Figure 8). In other words, stress changes in the shallow patch were more than an order of magnitude greater than stress changes in the deep patch. The southeastern shallow patch is marked by B in Figure 8, and the northwestern shallow patch is marked by C.

Static Coloumb stress changes from nearby earthquakes have been suggested to either hinder [*Wallace et al.*, 2014] or enhance [*Hirose et al.*, 2012] SSE generation. In the case of the 2013–2014 Kapati, New Zealand, SSE, a large change in ΔCFS following a *M* 6.4 intraslab normal faulting earthquake halted the

SSE [*Wallace et al.*, 2014]. ΔCFS induced by the Tohoku earthquake in the area of the 2011 Boso SSE (Japan) was on the order of 0.1 MPa [*Hirose et al.*, 2012; *Liu et al.*, 2015]ʹ. The Boso event recurrence time was advanced by an amount proportional to ΔCFS relative to its usual stress drop [*Hirose et al.*, 2012].

These observations are limited to small stress changes due to either a small nearby earthquake or a large distant event. If we take the shallow and deep SSE in Nicoya as separate events, we can calculate their average stress drop [*Hirose et al.*, 2012]:

$$\Delta\sigma \sim 2.5 M_o / S^{1.5}$$

where $\Delta\sigma$ is the stress drop, M_o is the SSE moment, and S is the slip area. The deep patch has an average stress drop of ~0.01 MPa, while the shallow event has an average stress drop of ~0.006 MPa. The deep SSE patch experienced a stress increase from the earthquake on the order of its typical stress drop, while the shallow patch experienced a stress increase from the earthquake many orders of magnitude greater than its usual stress drop. These stress drops are calculated using slip distributions from a homogeneous half-space, which may underestimate the offshore slip [*Williams and Wallace*, 2015]. The Nicoya earthquake should have caused a temporary decrease in the recurrence rate for Nicoya SSEs according to the model of *Hirose et al.* [2012]. However, the deep patch seems to be unaffected, while the recurrence time for the shallow patch appears to have increased (assuming this behavior continues), opposite to that expected from our simple ΔCFS calculations, this suggests that the process controlling SSE behavior is not solely controlled by stress state. It should be noted that the previous calculations are highly dependent on the slip estimates for the individual events (both SSE and the earthquake) which contain significant uncertainty offshore as resolution decreases and is further discussed in section 9 (Figure S3).

9. Discussion

It seems likely that conditions in the shallow SSE patch were sufficiently altered by the earthquake from the original "conditionally stable" state, such that subsequent slow slip was temporarily precluded. Afterslip mainly extended updip and along strike from the main earthquake rupture [*Malservisi et al.*, 2015], causing larger changes within the shallow SSE region compared to the deeper SSE region. Inversions place afterslip as shallow as the boundary of previously identified SSE [*Malservisi et al.*, 2015], and afterslip may extend all the way to the trench [*Hobbs et al.*, 2017]. This provides considerable uncertainty regarding the validity of our coulomb stress calculation, which is dependent on the earthquake slip distribution as inverted from the onshore GPS network. If afterslip does extend from the earthquake epicenter to the trench this would greatly reduce the coulomb stress with the shallow SSE patch, and it may even be negative. However, our afterslip estimates do not require significant slip within the shallow SSE patch given the available observations. Stress calculations are further complicated by consideration of rheologically dependent postseismic behavior such as viscoelastic relaxation. GPS along the peninsula have not returned to their preseismic velocity as of the 2015 SSE implying that postseismic processes (possibly both afterslip and viscoelastic relaxation) may be ongoing and partially affect both location and magnitude of the observed SSE.

The behavior of the 2014 SSE is consistent with the concept that deep and shallow SSEs are fundamentally different [e.g., *Saffer and Wallace*, 2015]. The deep patch appears to display time predictable behavior throughout the earthquake cycle. It is located downdip of an asperity that ruptures every ~50 years, possibly associated with subduction of the Fisher seamount chain [*Protti et al.*, 1995]. The location of this seamount may be controlling deep SSE location [*Dixon et al.*, 2014]. Behavior of the shallow patch is less clear. A simple conceptual model distinguishes the behavior of these two patches based on the source, volumes, and possible role of fluids that may be responsible for transient slip behavior. The deep patch is associated with fluids from slab dehydration associated with metamorphic phase reactions [*Rogers and Dragert*, 2003; *Szeliga et al.*, 2004], a process that may be relatively constant throughout the earthquake cycle and may have relatively low volumes and fluxes. Fluids generated near the shallow patch are controlled by compaction and dehydration of subducting sediments, likely distributed heterogeneously throughout the megathrust, and with potentially higher volumes, fluxes, and variability [*Saffer and Wallace*, 2015]. The higher permeability associated with the shallow subduction zone experiences greater changes during earthquakes and afterslip and hence requires more time to heal compared to the less permeable deep subduction zone [e.g., *Audet et al.*, 2009].

The apparently fragile nature of the shallow SSE zone identified here may explain why deep SSEs are identified in many subduction zones, while shallow SSEs are much less common. However, shallow SSE are difficult to assess using onshore instrumentation, potentially creating an observation bias. Alternatively, our observation period is too short to have documented the full spectrum of SSE behavior in Nicoya.

Stress interaction, as the slip front moves downdip, between the zones allows for both patches to slip simultaneously but does not require it, as was the case during the 2011 shallow SSE [*Dixon et al.*, 2014] and 2014 deep event. In addition, different time-dependent behavior is seen at inland stations compared to coastal stations (Figure S2). Inland stations generally observe a longer duration signal than coastal stations, which are impulsive. This may indicate that the deep slip patch in 2014 and 2015 had lower slip rates with longer slip durations than the shallow patches. Alternatively, rheological differences near the transition zone contribute to the longer duration at the inland stations. Interaction between the two patches may have occurred in the 2007 SSE, in which coastal stations responded first, hinting that the shallow slow slip patch slipped before the deep patch [*Outerbridge et al.*, 2010; *Jiang et al.*, 2017]. Future observations may provide additional insight into these relationships. In particular, frequent observations of offshore strain accumulation are important, as this region appears to be more variable. Improved understanding of these temporally variable locking and strain release patterns [e.g., *Frank*, 2016; *Melnick et al.*, 2017] throughout the earthquake cycle may allow better forecasts of earthquake hazard and tsunami.

10. Conclusions

We describe two SSEs that occurred in 2014 and 2015 in the early part of the earthquake cycle in the northern Costa Rica subduction zone. These events took place simultaneously with significant postseismic deformation associated with the 2012 *M* 7.6 earthquake. The recurrence rate of the deep SSEs in the Nicoya region was unchanged despite the large earthquake. The 2014 SSE is predominately a deep (40 km) slip event with the slip of shallow region normally active in previous events significantly reduced or not present. This is a significant change from preearthquake SSEs, all of which included considerable shallow slip at depth of around 15 km depth. The 2015 event was significantly larger than pre-earthquake SSEs, and shallow slow slip returned. This indicates that slip distributions from SSEs in Nicoya are not constant throughout the earthquake cycle, generating uncertainty in the long term strain accumulation.

References

Allen, M. R., and A. W. Robertson (1996) Distinguishing modulated oscillations from coloured noise in multivariate datasets, *Clim. Dyn.*, *12*(11), 775–784, doi:10.1007/s003820050142.

Audet, P., M. G. Bostock, N. I. Christensen, and S. M. Peacock (2009), Seismic evidence for overpressured subducted oceanic crust and megathrust fault sealing, *Nature*, *457*(7225), 76–78, doi:10.1038/nature07650.

Aster R. (2013), *In Parameter Estimation and Inverse Problems*, 2nd ed., edited by B. Borchers and C. H. Thurber, pp. 240–252, Academic Press, Boston, doi:10.1016/B978-0-12-385048-5.00031-8.

Bassiri, S., and G. A. Hajj (1993), Higher-order ionospheric effects on the global positioning system observables and means of modeling them, *Manuscr. Geodaet.*, *18*(5), 280–280.

Bertiger, W., S. D. Desai, B. Haines, N. Harvey, A. W. Moore, S. Owen, and J. P. Weiss (2010), Single receiver phase ambiguity resolution with GPS data, *J. Geod.*, *84*(5), 327–337, doi:10.1007/s00190-010-0371-9.

Boehm J., B. Werl, and H. Schuh (2006), Troposphere mapping functions 296 for GPS and very long baseline interferometry from European Centre for 297 Medium-Range Weather Forecasts operational analysis data, *J. Geophys. Res.*, *111*, B02406, doi:10.1029/2005JB003629.

Broomhead, Dr S., and G. P. King (1986), Extracting qualitative dynamics from experimental data, *Physica D*, *20*(2–3), 217–236, doi:10.1016/0167-2789(86)90031-X.

Chakravarty, I. M., J. D. Roy, and R. G. Laha (1967), *Handbook of Methods of Applied Statistics*, pp. 392–394, John Wiley, New York.

Chen, Q., T. van Dam, N. Sneeuw, X. Collilieux, M. Weigelt, and P. Rebischung (2013), Singular spectrum analysis for modeling seasonal signals from GPS time series, *J. Geodyn.*, *72*, 25–35, doi:10.1016/j.jog.2013.05.005.

Colella, H. V., J. H. Dieterich, K. Richards-Dinger, and A. M. Rubin (2012), Complex characteristics of slow slip events in subduction zones reproduced in multi-cycle simulations, *Geophys. Res. Lett.*, *39*, L20312, doi:10.1029/2012GL053276.

Davis, E. E., and H. W. Villinger (2006), Transient formation fluid pressures and temperatures in the Costa Rica forearc prism and subducting oceanic basement: CORK monitoring at ODP sites 1253 and 1255, *Earth Planet. Sci. Lett.*, *245*(1), 232–244, doi:10.1016/j.epsl.2006.02.042.

Davis, E., M. Heesemann, and K. Wang (2011), Evidence for episodic aseismic slip across the subduction seismogenic zone off Costa Rica: CORK borehole pressure observations at the subduction prism toe, *Earth Planet. Sci. Lett.*, *306*(3), 299–305, doi:10.1016/j.epsl.2011.04.017.

DeMets C. (2001), A new estimate for present day Cocos & Caribbean Plate motion: Implications for slip along the Central American Volcanic Arc, *Geophys. Res. Lett.*, *28*, 4043–4046, doi:10.1029/2001GL013518.

Dixon, T. H., Y. Jiang, R. Malservisi, R. McCaffrey, N. Voss, M. Protti, and V. Gonzalez (2014), Earthquake and tsunami forecasts: Relation of slow slip events to subsequent earthquake rupture, *Proc. Natl. Acad. Sci, U.S.A.*, *111*(48), 17,039–17,044, doi:10.1073/pnas.141229911.

Doherty, J. (2012), Pest: Model-independent parameter estimation and uncertainty analysis, 2010.

Doherty, J. E., and R. J. Hunt (2010), Approaches to highly parameterized inversion: A guide to using PEST for groundwater-model calibration, US Dep. of the Interior, U.S. Geol. Surv.

Dong, D., P. Fang, Y. Bock, F. Webb, L. Prawirodirdjo, S. Kedar, and P. Jamason (2006), Spatiotemporal filtering using principal component analysis and Karhunen-Loeve expansion approaches for regional GPS network analysis, *J. Geophys. Res.*, *111*, B03405, doi:10.1029/2005JB003806.

Douglas, A., J. Beavan, L. Wallace, and J. Townend (2005), Slow slip on the northern Hikurangi subduction interface, New Zealand, *Geophys. Res. Lett. 32*, L16305, doi:10.1029/2005GL023607.

Dragert, H., K. Wang, and T. S. James (2001), A silent slip event on the deeper Cascadia subduction interface, *Science*, *292*(5521), 1525–1528, doi:10.1126/science.1060152.

Feng, L., A. V. Newman, M. Protti, V. Gonzalez, Y. Jiang, and T. H. Dixon (2012), Active deformation near the Nicoya peninsula, northwestern Costa Rica, between 1996 and 2010: Interseismic megathrust coupling, *J. Geophys. Res.*, *117*, B06407, doi:10.1029/2012JB009230.

Frank, W. B. (2016), Slow slip hidden in the noise: The intermittence of tectonic release, *Geophys. Res. Lett.*, *43*, 10,125–10,133, doi:10.1002/2016GL069537.

Ghil, M., et al. (2002), Advanced spectral methods for climatic time series, *Rev. Geophys.*, *40*(1), 1003, doi:10.1029/2000RG000092.

Hayes, G. P., D. J. Wald, and R. L. Johnson (2012), Slab1.0: A three-dimensional model of global subduction zone geometries, *J. Geophys. Res. 117*, B01302, doi:10.1029/2011JB008524.

Hirose, H., H. Kimura, B. Enescu, and S. Aoi (2012), Recurrent slow slip event likely hastened by the 2011 Tohoku earthquake, *Proc. Natl. Acad. Sci. U.S.A.*, *109*(38), 15,157–15,161, doi:10.1073/pnas.1202709109.

Hobbs, T. E., C. Kyriakopoulos, A. V. Newman, M. Protti, and D. Yao (2017), Large and primarily updip afterslip following the 2012 M_w 7.6 Nicoya, Costa Rica, earthquake, *J. Geophys. Res. Solid Earth*, *122*, doi:10.1002/2017JB014035.

Ide, S., G. C. Beroza, D. R. Shelly, and T. Uchide (2007), A scaling law for slow earthquakes, *Nature*, *447*(7140), 76–79, doi:10.1038/nature05780.

Ito, Y., et al. (2013), Episodic slow slip events in the Japan subduction zone before the 2011 Tohoku-Oki earthquake, *Tectonophysics*, *600*, 14–26, doi:10.1016/j.tecto.2012.08.022.

Jiang, Y., S. Wdowinski, T. H. Dixon, M. Hackl, M. Protti, and V. Gonzalez (2012), Slow slip events in Costa Rica detected by continuous GPS observations, 2002–2011, *Geochem. Geophys. Geosyst.*, *13*, Q04006, doi:10.1029/2012GC004058.

Jiang, Y., Z. Liu, E. E. Davis, S. Y. Schwartz, T. H. Dixon, N. Voss, R Malservisi, and M. Protti (2017), Strain release at the trench during shallow slow slip: The example of Nicoya Peninsula, Costa Rica, *Geophys. Res. Lett.*, *44*, 4846–4854, doi:10.1002/2017GL072803.

Kedar, S., G. A. Hajj, B. D. Wilson, and M. B. Heflin (2003), The effect of the second order GPS ionospheric correction on receiver positions, *Geophys. Res. Lett.*, *30*(16), 1829, doi:10.1029/2003GL017639.

Kyriakopoulos, C., and A. V. Newman (2016), Structural asperity focusing locking and earthquake slip along the Nicoya megathrust, Costa Rica, *J. Geophys. Res. Solid Earth 121*, 5461–5476, doi:10.1002/2016JB012886.

Lambert, A., H. Kao, G. Rogers, and N. Courtier (2009), Correlation of tremor activity with tidal stress in the northern Cascadia subduction zone, *J. Geophys. Res.*, *114*, B00A08, doi:10.1029/2008JB006038.

Larson, K. M., V. Kostoglodov, S. Miyazaki, and J. Antonio, S. Santiago (2007), The 2006 aseismic slow slip event in Guerrero, Mexico: New results from GPS, *Geophys. Res. Lett.*, *34*, L13309, doi:10.1029/2007GL029912.

Liu, Z., A. W. Moore, and S. Owen (2015), Recurrent slow slip event reveals the interaction with seismic slow earthquakes and disruption from large earthquake, *Geophys. J. Int.*, *202*(3), 1555–1565, doi:10.1093/gji/ggv184.

Lowry, A. R., K. M. Larson, V. Kostoglodov, and R. Bilham (2001), Transient fault slip in Guerrero, southern Mexico, *Geophys. Res. Lett.*, *28*(19), 3753–3756, doi:10.1029/2001GL013238.

Lyard, F., F. Lefevre, T. Letellier, and O. Francis (2006), Modeling the global ocean tides: Modern insights from FES2004, *Ocean Dyn.*, *56*(5–6), 394–415, doi:10.1007/s10236-006-0086-x.

Malservisi, R., et al. (2015), Multiscale postseismic behavior on a megathrust: The 2012 Nicoya earthquake, Costa Rica, *Geochem. Geophys. Geosyst.*, *16*, 1848–1864, doi:10.1002/2015GC005794.

Mao, A., C. G. Harrison, and T. H. Dixon (1999), Noise in GPS coordinate time series, *J. Geophys. Res.*, *104*, 2797–2816, doi:10.1029/1998JB900033.

Matsuzawa, T., H. Hirose, B. Shibazaki, and K. Obara (2010), Modeling short-and long-term slow slip events in the seismic cycles of large subduction earthquakes, *J. Geophys. Res.*, *115*, B12301, doi:10.1029/2010JB007566.

Melnick, D., M. Moreno, J. Quinteros, J. C. Baez, Z. Deng, S. Li, and O. Oncken (2017), The super-interseismic phase of the megathrust earthquake cycle in Chile, *Geophys. Res. Lett.*, *44*, 784–791, doi:10.1002/2016GL071845.

Obara, K. (2002), Nonvolcanic deep tremor associated with subduction in southwest Japan, *Science*, *296*(5573), 1679–1681, doi:10.1126/science.1070378.

Obara, K., and A. Kato (2016), Connecting slow earthquakes to huge earthquakes, *Science*, *353*(6296), 253–257, doi:10.1126/science.aaf1512.

Okada, Y. (1992), Internal deformation due to shear and tensile faults in a half-space, *Bull. Seismol. Soc. Am.*, *82*(2), 1018–1040.

Outerbridge, K. C., T. H. Dixon, S. Y. Schwartz, J. I. Walter, M. Protti, V. Gonzalez, J. Biggs, M. Thorwart, and W. Rabbel (2010), A tremor and slip event on the Cocos-Caribbean subduction zone as measured by a global positioning system (GPS) and seismic network on the Nicoya Peninsula, Costa Rica, *J. Geophys. Res.*, *115*, B10408, doi:10.1029/2009JB006845.

Ozawa, S. (2014), Shortening of recurrence interval of Boso slow slip events in Japan, *Geophys. Res. Lett.*, *41*, 2762–2768, doi:10.1002/2014GL060072.

Protti, M., et al. (1995), The March 25, 1990 (M_w = 7.0, ML = 6.8), earthquake at the entrance of the Nicoya Gulf, Costa Rica: Its prior activity, foreshocks, aftershocks, and triggered seismicity, *J. Geophys. Res.*, *100*, 20,345–20,358, doi:10.1029/94JB03099.

Protti, M., V. González, T. Kato, T. Iinuma, S. Miyasaki, K. Obana, Y. Kaneda, P. LaFemina, T. Dixon, and S. Schwartz (2004), A creep event on the shallow interface of the Nicoya Peninsula, Costa Rica seismogenic zone, *Eos Trans. AGU*, *85*(47), Fall Meet. Suppl., Abstract S41D-0.

Protti, M., V. González, A. V. Newman, T. H. Dixon, S. Y. Schwartz, J. S. Marshall, L. Feng, J. I. Walter, R. Malservisi, and S. E. Owen (2014), Nicoya earthquake rupture anticipated by geodetic measurement of the locked plate interface, *Nat. Geosci.*, *7*(2), 117–121, doi:10.1038/ngeo2038.

Reasenberg, P. A., and R. W. Simpson (1992), Response of regional seismicity to the static stress change produced by the Loma Prieta earthquake, *Science*, *255*(5052), 1687–1690.

Rebischung, P., J. Griffiths, J. Ray, R. Schmid, X. Collilieux, and B. Garayt (2012), IGS08: The IGS realization of ITRF2008, *GPS Solutions*, *16*, 483–494, doi:10.1007/s10291-011-0248-2.

Rogers, G., and H. Dragert (2003), Episodic tremor and slip on the Cascadia subduction zone: The chatter of silent slip, *Science*, *300*(5627), 1942–1943, doi:10.1126/science.1084783.

Rubinstein, J. L., M. La Rocca, J. E. Vidale, K. C. Creager, and A. G. Wech (2008), Tidal modulation of nonvolcanic tremor, *Science*, *319*(5860), 186–189, doi:10.1126/science.1150558.

Saffer, D. M., and L. M. Wallace (2015), The frictional, hydrologic, metamorphic and thermal habitat of shallow slow earthquakes, *Nat. Geosci.*, doi:10.1038/ngeo2490.

Scholz, C. H. (1998), Earthquakes and friction laws, *Nature*, *391*(6662), 37–42, doi:10.1038/34097.

Schwartz, S. Y., and J. M. Rokosky (2007), Slow slip events and seismic tremor at circum-Pacific subduction zones, *Rev. Geophys.*, *45*, RG3004, doi:10.1029/2006RG000208.

Shen, Z. K., Q. Wang, R. Bürgmann, Y. Wan, and J. Ning (2005), Pole-tide modulation of slow slip events at circum-Pacific subduction zones, *Bull. Seismol. Soc. Am.*, *95*(5), 2009–2015, doi:10.1785/0120050020.

Stein, R. S., G. C. P. King, and J. Lin (1992), Change in failure stress on the southern San Andreas Fault system caused by the 1992 magnitude = 7.4 Landers earthquake, *Science*, *258*(5086), 1328–1332, doi:10.1126/science.258.5086.1328.

Szeliga, W., T. I. Melbourne, M. M. Miller, and V. M. Santillan (2004), Southern Cascadia episodic slow earthquakes, *Geophys. Res. Lett.*, *31*, L16602, doi:10.1029/2004GL020824.

Toda, S., R. S. Stein, V. Sevilgen, and J. Lin (2011), Coulomb 3.3 graphic-rich deformation and stress-change software for earthquake, tectonic, and volcano research and teaching user guide. [Available at http://usgsprojects.org/coulomb/Coulomb33of2011-1060.pdf.]

Unal, Y. S., and M. Ghil (1995), Interannual and interdecadal oscillation patterns in sea level, *Clim. Dyn.*, *11*(5), 255–278, doi:10.1007/BF00211679.

Vautard, R., and M. Ghil (1989), Singular spectrum analysis in nonlinear dynamics, with applications to paleoclimatic time series, *Physica D, Nonlinear Phenomena 35*(3), 395–424, doi:10.1016/0167-2789(89)90077-8.

Vautard, R., P. Yiou, and M. Ghil (1992), Singular-spectrum analysis: A toolkit for short, noisy chaotic signals, *Physica D*, *58*(1), 95–126, doi:10.1016/0167-2789(92)90103-T.

Wallace, L. M., N. Bartlow, I. Hamling, and B. Fry (2014), Quake clamps down on slow slip, *Geophys. Res. Lett.*, *41*, 8840–8846, doi:10.1002/2014GL062367.

Walwer, D., E. Calais, and M. Ghil (2016), Data-adaptive detection of transient deformation in geodetic networks, *J. Geophys. Res. Solid Earth*, *121*, 2129–2152, doi:10.1002/2015JB012424.

Williams, C. A., and L. M. Wallace (2015), Effects of material property variations on slip estimates for subduction interface slow-slip events, *Geophys. Res. Lett.*, *42*, 1113–1121, doi:10.1002/2014GL062505.

Wdowinski, S., Y. Bock, J. Zhang, P. Fang, and J. Genrich (1997), Southern California permanent GPS geodetic array: Spatial filtering of daily positions for estimating coseismic and postseismic displacements induced by the 1992 Landers earthquake, *J. Geophys. Res. 102*, 18,057–18,070, doi:10.1029/97JB01378.

Xue, L., S. Schwartz, Z. Liu, and L. Feng (2015), Interseismic megathrust coupling beneath the Nicoya Peninsula, Costa Rica, from the joint inversion of InSAR and GPS data, *J. Geophys. Res. Solid Earth*, *120*, 3707–3722, doi:10.1002/2014JB011844.

Yue, H., T. Lay, S. Y. Schwartz, L. Rivera, M. Protti, T. H. Dixon, and A. V. Newman (2013), The 5 September 2012 Nicoya, Costa Rica M_w 7.6 earthquake rupture process from joint inversion of high-rate GPS, strong-motion, and teleseismic P wave data and its relationship to adjacent plate boundary interface properties, *J. Geophys. Res. Solid Earth*, *118*, 5453–5466, doi:10.1002/jgrb.50379.

Zumberge, J. F., M. B. Heflin, D. J. Jefferson, M. M. Watkins, and F. H. Webb (1997), Precise point positioning for the efficient and robust analysis of GPS data from large networks, *J. Geophys. Res.*, *102*, 5005–5017, doi:10.1029/96JB03860

Zwillinger, D., and S. Kokoska (1999), *CRC Standard Probability and Statistics Tables and Formulae*, pp. 346–350, CRC Press, Boca Raton, Fla.